

Exploring the Ligand Functionality, Electronic Band Gaps, and Switching Characteristics of Single Wells–Dawson-Type Polyoxometalates on Gold

Maria Glöß, Ricarda Pütt, Marco Moors, Emmanuel Kentzinger, Silvia Karthäuser,* and Kirill Yu. Monakhov*

The miniaturization, high performance, energy efficiency, and new added functionalities are the essential drivers of modern information data storage and processing technologies. Polyoxometalates (POMs) characterized by atomically well-defined structures with discrete energy levels and the ability to undergo redox transformations are viewed as promising active components for the integration into the next-generation (beyond-CMOS) hybrid nanoelectronics. Herein, new fundamental insights into the application of organically augmented POMs on conducting surfaces are offered. Three key findings resulting from scanning probe investigations combined with integral spectroscopic methods used to explore tris(alkoxo)-ligated, vanadium-containing Wells-Dawson-type POM structures on Au(111) are reported on. First, it is shown how the $(\text{OCH}_2)_3\text{C-R}$ ligands, depending on the structurally exposed R group ($\text{R} = \text{CH}_2\text{SMe}$ and $\text{NHCO}_2\text{C}_6\text{H}_4\text{SMe}$), influence the self-assembly behavior of the synthesized POMs on gold. Second, the impact of the employed $(\text{OCH}_2)_3\text{C-R}$ ligands and the determined assembly characteristics on the relative position of POM's electronic band structure against the Fermi level of the gold surface are explained. Third, the on-surface conductance switching of single POM structures due to external electrical stimuli is demonstrated. The author's experimental efforts enable to discover highly sought-after multi-level resistive switching orchestrated by electrically accessible $\text{V}(3d)$ states in the POM single-molecules at room temperature in a narrow voltage range.

1. Introduction

The continuous decrease of the feature size in complementary metal-oxide-semiconductor (CMOS) devices during the last decades, in line with the “Moore law” predicting a doubling of the transistor number on integrated circuits at least every two years,^[1] has led to a tremendous increase of efficiency in data storage and processing. However, the actual and future challenges in information and communication technology, including downscaling to a very few nanometers, switching at lower power, higher density capacitive data storage, in-memory computing,^[2] etc., illustrate the need for novel scalable beyond-CMOS device concepts.^[3] In their development the search from the bottom up for high-performance materials as active electronic components and for new switching mechanisms takes a central role.


Molecular electronics^[4] exploiting the chemical functionality with the physical state variables such as charge and spin has emerged to enable not only further

M. Glöß, M. Moors, K. Y. Monakhov
Leibniz Institute of Surface Engineering (IOM)
Permoserstraße 15, 04318 Leipzig, Germany
E-mail: kirill.monakhov@iom-leipzig.de

M. Glöß, S. Karthäuser
Peter Grünberg Institut (PGI-7)
JARA-FIT
Forschungszentrum Jülich GmbH
Wilhelm-Johnen-Straße
52425 Jülich, Germany
E-mail: s.karthauser@fz-juelich.de

R. Pütt
Institute of Inorganic Chemistry
RWTH Aachen University
Landoltweg 1, 52074 Aachen, Germany

E. Kentzinger
Jülich Centre for Neutron Science (JCNS) and Peter Grünberg
Institute (PGI)
JARA-FIT
Forschungszentrum Jülich GmbH
Wilhelm-Johnen-Straße
52425 Jülich, Germany

 The ORCID identification number(s) for the author(s) of this article can be found under <https://doi.org/10.1002/admi.202200461>.

© 2022 The Authors. Advanced Materials Interfaces published by Wiley-VCH GmbH. This is an open access article under the terms of the Creative Commons Attribution-NonCommercial-NoDerivs License, which permits use and distribution in any medium, provided the original work is properly cited, the use is non-commercial and no modifications or adaptations are made.

DOI: 10.1002/admi.202200461

downscaling^[5] to a sub-molecular level but also a perspective on the integration of controllable switching variables at the atomic level,^[6] especially in the context of resistive^[7] memories (ReRAM). In contrast to classical charge-based memories (Flash or DRAM), ReRAMs are characterized by the change of electrical conductance as a function of an applied electrical potential.^[7–9] ReRAMs offer several key advantages, in particular high scalability, high efficiency, and low production costs, due to their rather simple “metal//insulator//metal” structure.^[10,11] In combination with the non-volatile data storage and the principal ability for multi-level switching, resistive memories are not only suitable for conventional computing devices (e.g., as successor to Flash memories in solid-state discs), but are also highly appealing for radically new research directions such as neuromorphic computing.^[12,13] The physical mechanisms of resistive switching are rather complex and manifold, strongly depending on the used materials for electrodes and switching layers and on the switching conditions.^[10,14,15] In common ReRAM cells often thin films of redox-active transition metal oxides with extended solid-state structures are exploited as active switching layers,^[16] and in principle, they can be scaled down to the low nanometer level.^[6]

The combination of ReRAMs with stimuli-responsive molecular compounds such as negatively charged metal–oxo clusters (polyoxometalates, POMs)^[17,18] can have direct impact on the development of beyond-CMOS technology. Especially, archetypal POMs as building blocks,^[19] capable of versatile functionalization and derivatization by organic ligands,^[20,21] have emerged as excellent candidates to enable POM-based electronics^[22–24] due to highly efficient immobilization on surfaces,^[25,26] which is however limited to the molecular deposition from solution. In the context of POM-based resistive memories different approaches have been employed: 1) devices based on redox-active layers made up of POMs that are embedded in an organic polymer matrix^[9,27] or spin-casted^[28] from solution on a rigid surface; 2) characterization of on-surface immobilized single POM molecules exhibiting conductance switching as a function of V(3d) states addressed in a scanning tunneling microscope (STM).^[29]

Herein, we take a step forward and explore the self-assembly, electronic band gaps, and potential-induced switching of two ligated, V₃-substituted Wells–Dawson-type POMs as intact single molecules on the Au(111) surface. The Wells–Dawson-type structure belongs to archetypal POMs, enabling controlled tailoring of the ligand functionality (commonly postfunctionalization of tris(alkoxo) ligand^[20,21]) and an atom-specific modification of the POM core itself. Among a wide variety of POMs, Wells–Dawson-type POMs provide a suitable, stable scaffold to incorporate redox-active vanadium centers. The latter have been shown in our previous study^[29] to be electrically accessible by applying external potentials to a Lindqvist-type hexavanadate structure on the Au(111) surface. The combination of these structure–property features make vanadium-substituted Wells–Dawson-type POMs excellent candidates, alongside Lindqvist-type POMs, to study the underlying surface-physics phenomena of POMs at the level of single molecules. Special attention in the current study is paid to the effects of the chain length, the degree of substitution and thus, the overall electron-donating ability of POM’s tris(alkoxo) ligands (OCH₂)₃C–R (R = CH₂SMe versus R = NHCOC₆H₄SMe) on the on-surface adsorption characteristics and the electronic structure properties of these organic–inorganic hybrid compounds. The insights were gained best in the established two-terminal memory

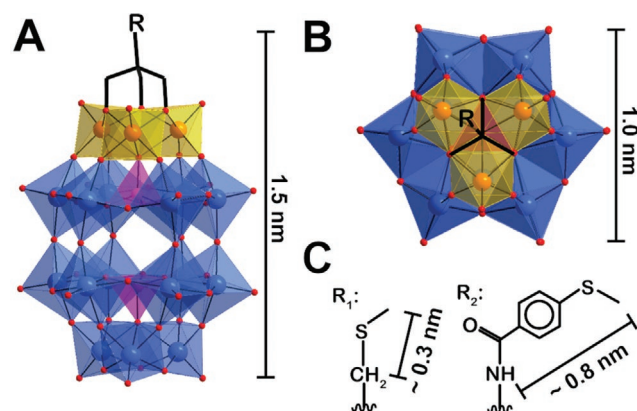


Figure 1. The (OCH₂)₃C–R ligated WD polyoxoanion. A) Side view. B) Top view. C) Ligand scaffolds: R₁ = CH₂SMe of WDS-1 and R₂ = NHCOC₆H₄SMe of WDS-2. Color code: blue octahedra = WO₆, yellow octahedra = VO₆, magenta square pyramids = PO₄, red spheres = O. H atoms are not shown.

cell test structure^[30] given by a STM, enabling scanning tunneling spectroscopy (STS) on well-defined positions over single POMs. The results are additionally supported by real-space surface imaging with atomic force microscopy (AFM), X-ray photoelectron spectroscopy (XPS), X-ray reflectivity (XRR), and grazing incidence small angle X-ray scattering (GISAXS) techniques.

2. Results and Discussion

2.1. Wet-Chemical Preparation of (TBA)₅WDS-1 and (TBA)₅WDS-2

The title (TBA)₅WDS-1 and (TBA)₅WDS-2 compounds (tBu₄N)₅[HP₂V₃W₁₅O₅₉((OCH₂)₃C–R)] consist of a tris(alkoxo)-ligated Wells–Dawson-type (WD) polyoxoanion component (Figure 1) with R = CH₂SMe or NHCOC₆H₄SMe, respectively, which is charge-balanced by five tBu₄N⁺ (TBA) counteranions. The compounds were synthesized according to the general synthetic procedure exploited in our previous study,^[31] that is, by reacting the (TBA)₅[H₄P₂V₃W₁₅O₆₂] archetype ((TBA)₅WD) with 2-(hydroxymethyl)-2-((methylthio)methyl)propane-1,3-diol (S-1) and N-[1,3-dihydroxy-2-(hydroxymethyl)propan-2-yl]-4-methylsulfanylbenzamide (S-2), respectively.^[29,32] Both compounds were obtained in high yields, 75% for (TBA)₅WDS-1 and 82% for (TBA)₅WDS-2. The details of their full characterization by elemental CHN analysis, infrared (IR) and nuclear magnetic resonance (⁵¹V-NMR and ³¹P-NMR) spectroscopy and electrospray ionization mass spectrometry (ESI-MS) can be found in the Supporting Information. For all the surface-related experiments with these compounds freshly prepared, water-free acetonitrile (MeCN) solutions were utilized to avoid (hierarchical) agglomeration of POMs, which was the subject of our previous study.^[31]

2.2. XPS of (TBA)₅WDS-1 and (TBA)₅WDS-2 on Au(111)

XPS analysis with the focus on tungsten and vanadium core levels was performed to verify the oxidation states of WDS-1 and WDS-2 adsorbed from MeCN solution on the gold surface (for details of molecular deposition see Section 4).

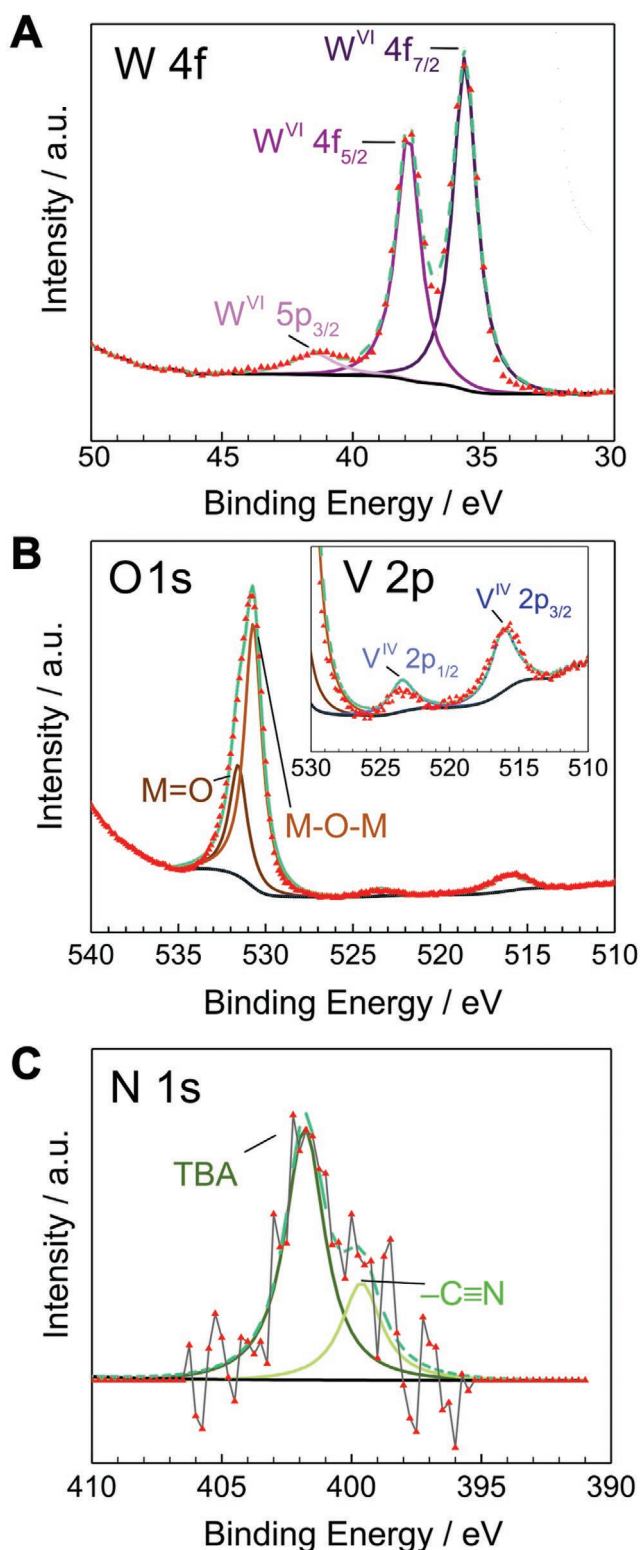


Figure 2. The XPS core-level spectra of WDS-1 on Au(111). A) W 4f; B) O 1s and V 2p (enlarged in inset); C) N 1s.

Figure 2 illustrates the W 4f, V 2p, O 1s, and N 1s core level regions of WDS-1. The XPS spectra of (TBA)₅WDS-1 and (TBA)₅WDS-2 are characterized by almost equal binding energies for all core levels (XPS of WDS-2 is given in

Figure S4, Supporting Information). The W 4f core level region (Figure 2A) exhibits one peak attributed to a W 5p_{3/2} signal and a well-separated W 4f doublet with an area ratio of 4:3 and a separation $\Delta = (2.2 \pm 0.2)$ eV between the 4f_{7/2} and the 4f_{5/2} signal. The characteristic maximum in intensity for the W 4f_{7/2} peak is determined at a binding energy of (35.7 ± 0.1) eV, and all W signals indicate a fully-oxidized tungsten W^{VI}.^[33]

The O 1s and V 2p core levels are depicted in Figure 2B. The deconvolution of the O 1s peak results in two oxygen components. The first maximum at (531.57 ± 0.06) eV is associated with double-bonded oxygen (M=O), while the second maximum at (530.70 ± 0.06) eV can be assigned to M–OH or M–O–M.^[34,35] The ratios of the two oxygen species is equal for both compounds and amounts to 1 : 2.4 equivalent to the ratio of O_{M=O}:O_{M–O–M} in the derivatives. The vanadium doublet has an area ratio of 1 : 2 and a separation $\Delta = (731 \pm 0.12)$ eV. The V 2p_{3/2} component arises at (516.13 ± 0.06) eV and corresponds to one vanadium species. The position of the V 2p_{3/2} peak with respect to the O 1s component ($\Delta E_{\text{WDS-1}} = (14.57 \pm 0.12)$ eV) points out a reduced vanadium V^{IV}.^[30,36]

Figure 2C shows the N 1s core level region with two binding energies. One maximum is observed at (401.8 ± 0.1) eV and assigned to the quaternary ammonium cation TBA.^[34] Another maximum appears at (399.6 ± 0.1) eV, which results from nitrile of residual solvent MeCN^[37] (and/or from amide^[38] in the ligand of WDS-2, see Figure S4C, Supporting Information). Notably, the intensity of the binding energy at 399.6 eV in the case of WDS-2 is higher than that for WDS-1. This clearly indicates the contribution of the amide group to this N 1s peak, as expected from the chemical structure (see Figure 1).

Overall, from these data the reduction of the vanadium centers^[39] from V^V to V^{IV} in the V₃ cap of the polyoxoanions for both compounds (TBA)₅WDS-1 and (TBA)₅WDS-2 on the Au(111) surface can be concluded. An analogous reduction of transition metal atoms was noted in the studies of Wells–Dawson tungstates ((NH₄)₆P₂W₁₈O₆₂) and molybdates ((NH₄)₆P₂Mo₁₈O₆₂) on aluminum surfaces.^[40] In the respective POMs the lowest unoccupied molecular orbital (LUMO) lies energetically lower than the Fermi energy (E_F) of the aluminum surface, and it can thus be populated by electrons from the metal. In the case of our compounds, the relevant Fermi energy of Au(111) is $E_F = -5.31$ eV,^[41] while the LUMO of ligand-free H₉[P₂V₃W₁₅O₆₂] is -5.2 eV as deduced from combined cyclic voltammetry and optical measurements.^[42] Obviously, the E_F of Au(111) and the estimated LUMO level of the ligand-free, fully protonated POM exhibit very close numbers. That prompted us to investigate in detail the influence of the tris(alkoxo) ligands (OCH₂)₃C–R with distinct electron-donating abilities ($R = \text{CH}_2\text{SMe}$ vs $\text{NHCOC}_6\text{H}_4\text{SMe}$, see Figure 1) on the interfacial alignment of the metallic Fermi level, given by Au(111), and the molecular orbital levels of WDS-1 and WDS-2.

2.3. Immobilization of (TBA)₅WDS-1 and (TBA)₅WDS-2 on Au(111)

The topography of both compounds on Au(111) was characterized by atomic force microscopy (AFM) in non-contact mode, which enables to investigate insulating samples. The distribution of (TBA)₅WDS-1 on Au(111) is illustrated in Figure 3 and reveals

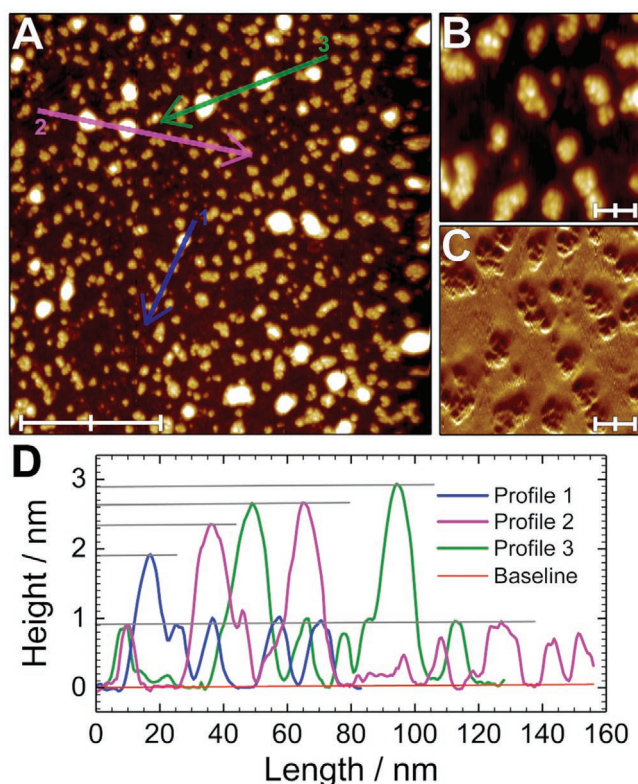


Figure 3. AFM images of $(\text{TBA})_5\text{WDS-1}$ on $\text{Au}(111)$ with the corresponding height profiles. A) Overview image. The colored arrows mark the height profiles (scale bar: 100 nm). B) High resolution image (scale bar: 10 nm). C) Corresponding phase image to (B). D) Height profiles along arrows in (A) (baseline in red).

a large number of small islands with varying size and height. The height of the small islands is varying stepwise, that is, the smallest assemblies of WDS-1 with (0.9 ± 0.1) nm dominate. Other islands with heights of (1.8 ± 0.2) nm and (2.7 ± 0.3) nm, corresponding to two or three times the basic height, are present in a smaller amount. The image section with a higher resolution is shown in Figure 3B and the corresponding phase image in Figure 3C. From these images it is deduced that the islands are formed from small round-shaped particles. These particles have a diameter of ≈ 2 nm, and they are identified as single WDS-1 polyoxoanions (see Figure 1) based on a comparison to the reported crystallographic data^[43] of similar Wells-Dawson-type POMs. As a result, WDS-1 is determined to adsorb as single units or to assemble as a group of polyoxoanions on $\text{Au}(111)$.

A high-resolution AFM image of $(\text{TBA})_5\text{WDS-2}$ on $\text{Au}(111)$ is presented in Figure 4A, the corresponding phase image in Figure 4B, and the height profiles in Figure 4C. In contrast to WDS-1, the assembly of WDS-2 exhibits an almost uniform height. A height of (1.1 ± 0.1) nm is obtained over large areas of assembled WDS-2 polyoxoanions and corresponds well to the small diameter of the POM anion, so that the longer organic ligands of neighboring WDS-2 can approach each other and/or the $\text{Au}(111)$ surface. Due to the amide group and the inherent large flexibility of S-2 the formation of hydrogen bonds between WDS-2 polyoxoanions can be anticipated, and the self-assembly of WDS-2 POMs is most likely directed by these

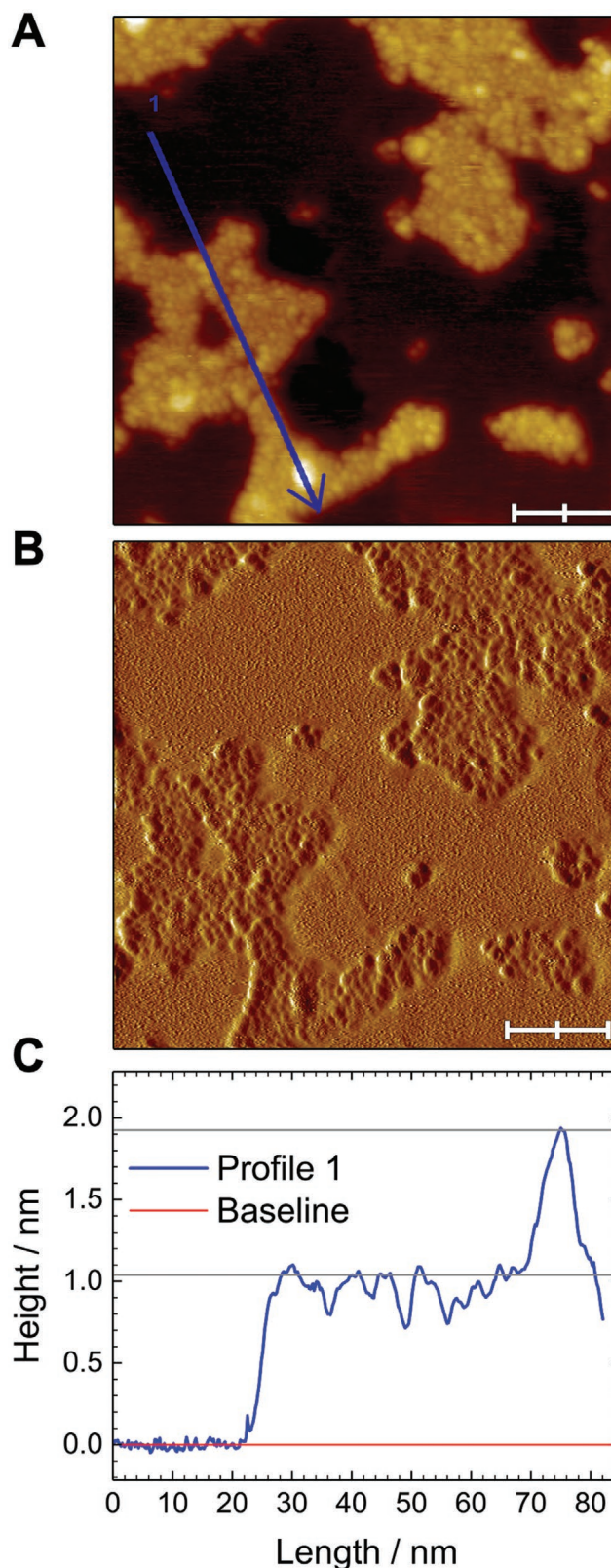


Figure 4. AFM images of $(\text{TBA})_5\text{WDS-2}$ on $\text{Au}(111)$. A) High resolution image (scale bar: 20 nm). The colored arrow marks the height profile. B) Phase image corresponding to (A). C) Height profile along the arrow in (A) (baseline in red).

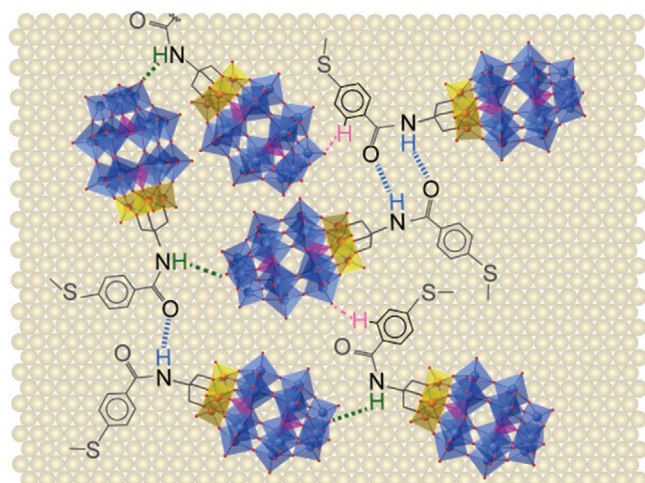


Figure 5. A model of the self-assembly of WDS-2 polyoxoanions on Au(111). Three different types of hydrogen bonds are depicted. Color code: blue = strong N—H...O bond between neighboring ligands, green = N—H...O—W bond between POM and neighboring ligand, pink = weak C—H...O—W bond between POM and a neighboring ligand involving a hydrogen at the 4-methylsulfanylbzamide ring.

weak interactions. In addition, it is stabilized by the thioether group -SMe which enhances the POM–Au(111) contact. Only a few points within the assemblies in Figure 4A show heights of (1.9 ± 0.2) nm corresponding to twice the basic height. Despite the alike polyoxoanion size of WDS-1 and WDS-2 their self-assembly behavior differs considerably on the metallic surface. This indicates a dissimilar character of POM–surface and POM–POM interactions triggered by the tris(alkoxo) ligands and, furthermore, the different ability of these POM-based organic–inorganic hybrids to form hydrogen bonds. A model of the hydrogen bond directed self-assembly of the WDS-2 polyoxoanions on gold is illustrated in **Figure 5**.

It is noteworthy that the importance of hydrogen bonding for the self-assembly of tris(alkoxo)-supported Wells–Dawson-type POMs was also reported by Cronin and co-workers,^[43] however

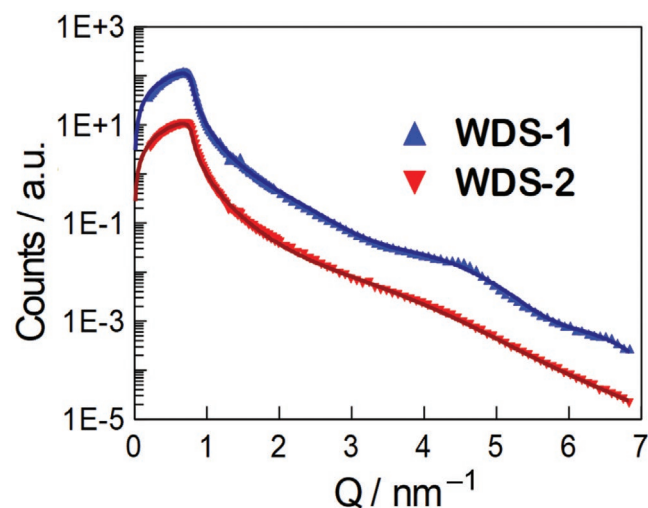


Figure 6. X-ray reflectivity as a function of scattering wavevector Q . For clarity, the data of WDS-1 are scaled by a factor of 10. The solid curves are fits to the data within the Parratt formalism.^[44]

in the context of crystal structure. The authors described a tetrameric POM structure, which is formed due to hydrogen bonds between the amino group of a $(\text{OCH}_2)_3\text{CNH}_2$ ligand and an oxygen atom of the neighboring polyoxoanion. The gas-phase analysis by means of cryospray ionization mass spectroscopy confirmed these tetrameric species, along with trimers, dimers, and monomers. Interestingly, the structure of the POM ligated by a $(\text{OCH}_2)_3\text{CMe}$ ligand is characterized by only monomers, and the gas-phase analysis of this compound revealed monomers and dimers.

To verify the adsorption behavior of WDS-1 and WDS-2 on Au(111) on a larger length scale than available by AFM, we performed X-ray reflectivity (XRR) measurements (**Figure 6**). A two-layer system for WDS-1 with a height of 1.34(3) nm for the first and 1.48(3) nm for the second layer was thus determined. For WDS-2 one layer with a height of 1.60(5) nm was measured. Since reflectivity is an integral measurement method, which averages over the whole surface, these values must be interpreted. Especially the higher value for the layer thickness obtained from reflectivity of WDS-2 (1.60 nm) compared to AFM heights (1.1 nm) results from the averaging over the first layer and partly appearing POMs in the second layer. The same averaging accounts for the layer heights of WDS-1. However, here again the dominant influence of the ligand on the modified assembly behavior of WDS-1 compared to WDS-2 could be demonstrated.

Next, we obtained grazing incidence small angle scattering (GISAXS) from WDS-1 and WDS-2 to showcase a possible long-range on-surface ordering. The POM-covered samples showed additional signals with respect to the GISAXS from the bare

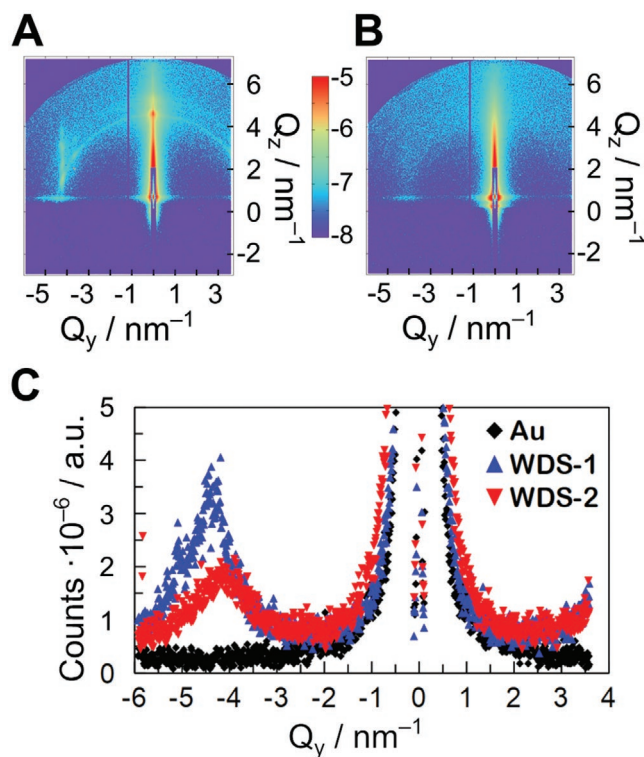


Figure 7. GISAXS from WDS-1 in (A) and WDS-2 in (B), measured at the same angle of incidence of the X-rays of 0.43° , close to the critical angle of total reflection. The intensities are on a logarithmic scale. C) Shows the GISAXS signals at $Q_z = 0.6 \text{ nm}^{-1}$ as a function of Q_y .

gold substrate (see Figure 7A,B, Figure S5, Supporting Information). In Figure 7C, slices at $Q_z = 0.6 \text{ nm}^{-1}$ are extracted. For WDS-1 and WDS-2, they show a pronounced peak at $Q_y = -4.5$ and -4.2 nm^{-1} , respectively. Those peaks correspond to the scattering from isolated and randomly distributed POMs on the surface. The positions of those peaks depend on the size, shape, and on the orientation of the POMs on the surface. However, due to the complexity of the ligated POMs used here, their exact shapes could not be assigned. Therefore, the determination of the sizes was abandoned.

Figure 7A illustrates some additional scattering along Q_z at Q_y around -4.3 nm^{-1} and along a ring of radius 4.5 nm^{-1} centered at the origin. This shows the tendency of a certain number of WDS-1 POMs to order in two and three dimensions. The modulated intensities along Q_z at $Q_y = -4.3 \text{ nm}^{-1}$ correspond to the scattering from a 2D in-plane powder of arrangements of POMs that order parallel and perpendicular to the surface. Such ordered arrangements are called “mesocrystals.”^[45] The ring of radius 4.5 nm^{-1} corresponds to the scattering from a 3D powder of such mesocrystals. An enhanced GISAXS signal from WDS-2 at $-1 < Q_y < 1 \text{ nm}^{-1}$, which agrees with Figure 4 depicting WDS-2 POMs covering large areas of the substrate, can be seen in Figure 7B,C. Overall, the XRR and GISAXS data confirm the very different in-depth and lateral orderings for both title POMs analyzed on the gold surface.

2.4. Determination of Electronic Band Gaps of WDS-1 and WDS-2 on Au(111)

The electronic band gaps of WDS-1 and WDS-2 were determined by taking a series of I - V spectra with the tip located above the respective single polyoxoanions. To control the integrity of the POMs during spectroscopy, STM images were performed before and after STS measurements. These small-area STM control-measurements of WDS-1 and WDS-2 (insets in Figures 8–10) were carried out at a large tip-sample distance (high bias voltage, low tunneling current) to avoid molecular displacements, which were observed otherwise (see overview images in Figures S7–S9, Supporting Information). The STM images are consistent with AFM images and depict assemblies of polyoxoanions with a comparable height and width, which are characteristic of single WDS-1 and WDS-2. For the latter POM, the STM images reveal a uniform height of the particles, and a few particles with the doubled height.

The I - V spectra in Figures 8–10 are averaged over ten individual I - V cycles recorded at one location. Figure 8A shows the I - V spectra (-1.5 to 1.5 V) obtained for single WDS-1 that were directly adsorbed as TBA salt on Au(111). The spectra were recorded with different set-points currents, that is, with different tip-sample distances, at the position marked in the inset. The logarithm of the absolute current was used to determine the electronic band gap (Figure 8B). For WDS-1 in direct contact with Au(111) the band gap $E_{G1}(\text{WDS-1})$ is calculated to be $(1.19 \pm 0.10) \text{ eV}$, with the conduction band (CB) edge $E_{CB1}(\text{WDS-1}) = 0.60 \text{ eV}$ and the valence band (VB) edge $E_{VB1}(\text{WDS-1}) = -0.59 \text{ eV}$. Figure 8C shows the height-normalized spectra according to the method of Feenstra.^[46] The absolute currents for each set-point are multiplied with $e^{(-2\kappa\Delta z)}$,

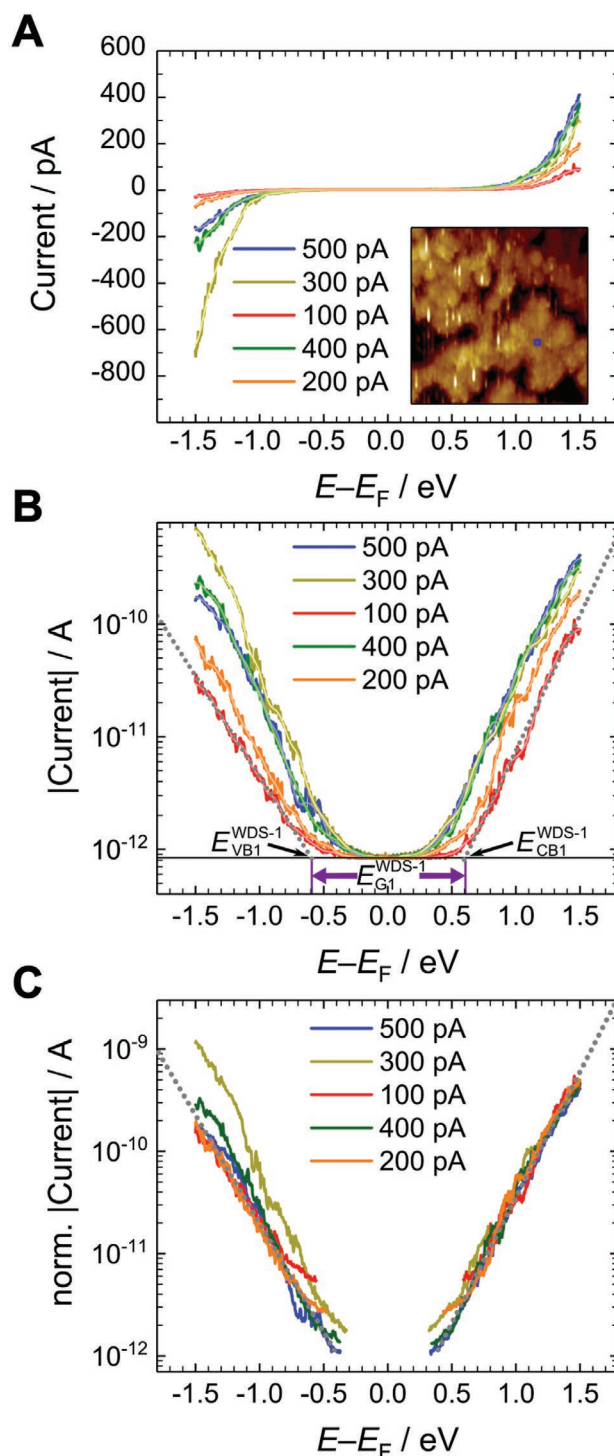


Figure 8. Tunneling spectra (STS) of WDS-1 directly adsorbed as TBA salt (first adsorption layer) on Au(111). A) Tunneling spectra recorded on single WDS-1 at different tip-sample distances defined by the set currents given in the legend and $U_B = 1.5 \text{ V}$. The inset shows the STM image ($50 \times 50 \text{ nm}^2$) of WDS-1 with the position of the tip for taking the I - V spectra marked by a blue point. B) Logarithmic presentation of the absolute current (deduced from (A)) used to determine the apparent band gap ($E_{G1}(\text{WDS-1})$), with $E_{CB1}(\text{WDS-1})$ conduction band edge and $E_{VB1}(\text{WDS-1})$ valence band edge. C) Height-normalized presentation of (B). The spectra were recorded in the order like given in the legend.

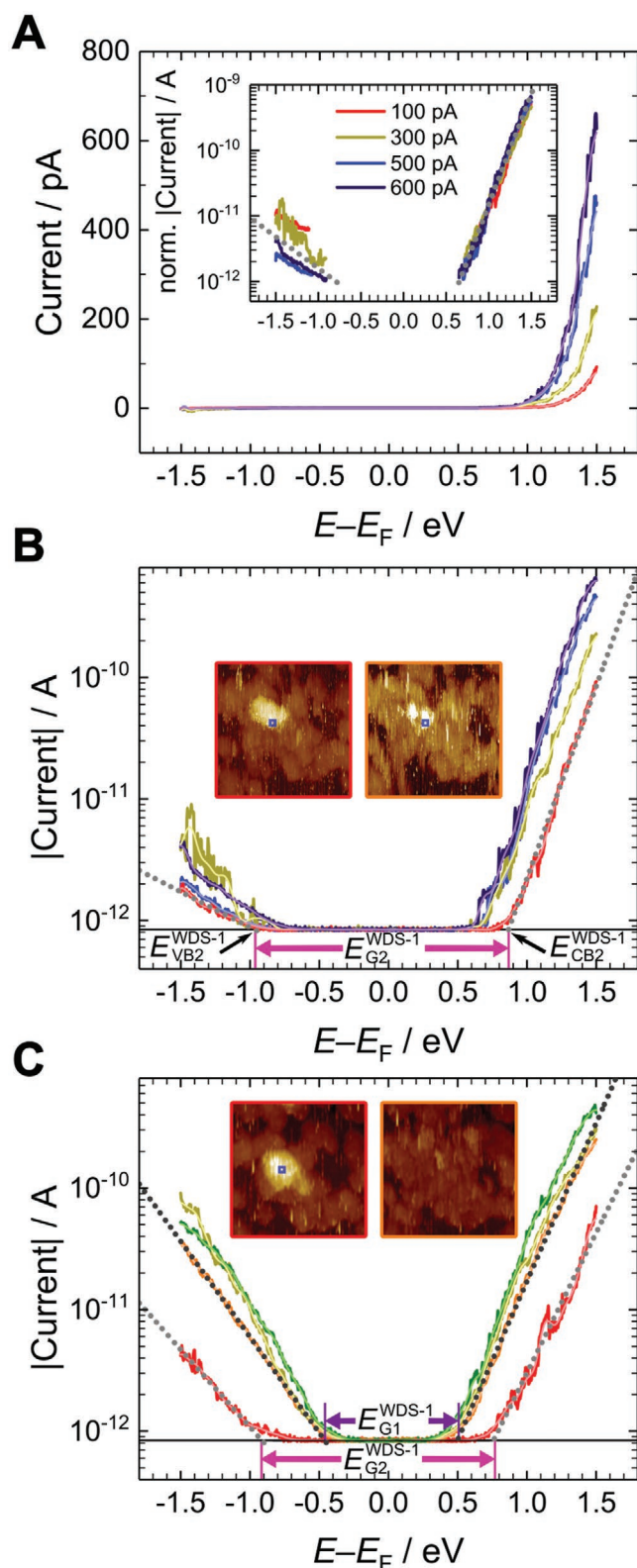


Figure 9. Tunneling spectra (STS) of WDS-1 polyoxoanions adsorbed in the second layer on Au(111) ($U_B = 1.5$ V). A) Tunneling spectra recorded at different tip-sample distances defined by the set current. The inset shows the height-normalized presentation of (A). B) Logarithmic presentations of the absolute current from (A). The insets show the position of WDS-1

where the inverse decay length amounts to $\kappa = 1.1 \text{ \AA}^{-1}$ (corresponding to the work function of tungsten, $\Phi_W = 4.5$ eV) and Δs is a difference between the tip-sample distance, defined by the respective set-point, and the reference height.

The I - V spectra of WDS-1 in the second layer differ from the spectra of these polyoxoanions directly adsorbed on Au(111). The spectra in **Figure 9A** showcase a distinct diode characteristic with a low current at the detection limit of the STM at a negative sample bias. The electronic band gap E_{G2} was determined according to the above-mentioned method to be (1.83 ± 0.09) eV (Figure 9B), with $E_{CB2}(\text{WDS-1}) = 0.86$ eV and $E_{VB2}(\text{WDS-1}) = -0.97$ eV. In contrast to WDS-1 in contact with Au(111), the band gap of WDS-1 in the second layer is considerably higher. For the latter one, the characteristics of the I - V curves indicate n-type semiconductor behavior.

A special case of abrupt transition in the I - V characteristics, which was recorded several times in a comparable manner, is presented in Figure 9C. The first spectrum at 100 pA exhibits the I - V characteristic of WDS-1 in the second layer, while the following measurements show the I - V characteristic of WDS-1 in direct contact with Au(111) marked by the considerable decrease of the band gap. This change in electrical properties can be directly correlated to the change in topography documented by the STM images that were taken before and after recording the I - V spectra (inset in Figure 9C). The particle of interest changed its position during the STS measurements. While the WDS-1 was adsorbed in the second layer initially, it was embedded into the first adsorption layer after completing the measurement series.

The STS spectra of WDS-2 are comparable to the spectra of WDS-1 in direct contact with Au(111) and the determined band gap is also nearly equal, $E_{G1}(\text{WDS-2}) = (1.17 \pm 0.15)$ eV, resulting from $E_{CB1}(\text{WDS-2}) = 0.65$ eV and $E_{VB1}(\text{WDS-2}) = -0.52$ eV (Figure 10).

The band gaps obtained for WDS-1 and WDS-2 directly adsorbed on Au(111) are considerably smaller than those obtained from theoretical calculations^[47] of tris(alkoxo)-ligated, fully-oxidized Wells-Dawson-type polyoxoanions having an alike POM composition. The theoretical band gaps of $[\text{P}_2\text{V}_3\text{W}_{15}\text{O}_{59}(\text{OCH}_2)_3\text{C-R}]^{6-}$ furnished with $\text{R} = \text{Me}$ and NH_2 correspond to $\Delta E_{\text{HOMO-LUMO}}$ of 1.94 and 1.52 eV, respectively. Based on the reported^[47] partial density of states plots, the energetic position of the LUMO, which is mainly located on the vanadium atoms, is considerably governed by the charge transfer from the tris(alkoxo) ligands to the V_3 -cap. The data of these density functional theory calculations^[47] can be linked to WDS-1 and WDS-2 as the $(\text{OCH}_2)_3\text{C-R}$ ligands ($\text{R} = \text{CH}_2\text{SMe}$ and $\text{NHC-OC}_6\text{H}_4\text{SMe}$, respectively) explored herein exhibit similar scaffolds and a rather comparable electron-withdrawing/-donating ability to the $(\text{OCH}_2)_3\text{C-R}$ ligands of the above-mentioned POMs with $\text{R} = \text{Me}$ and NH_2 . Interestingly, the theoretically

(marked blue) in the second layer ($50 \times 50 \text{ nm}^2$) before (red bordered image) and after (orange bordered image) STS measurements. C) A second characteristic set of tunneling spectra recorded on a particle in the second layer. Inset: STM image before and after the measurement. $E_{G1}(\text{WDS-1})$ and $E_{G2}(\text{WDS-1})$ are the electronic band gaps determined for WDS-1 from the first and the second adsorption layer, respectively. Color code like given in Figure 8.

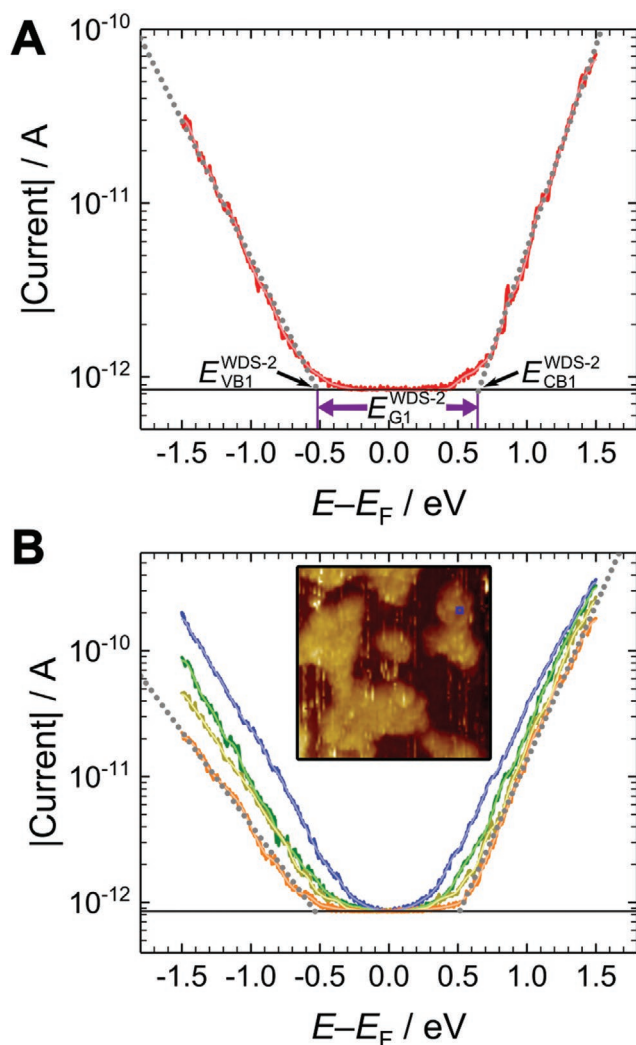


Figure 10. Tunneling spectra (STS) of WDS-2 directly adsorbed as TBA salt on Au(111). A) Tunneling spectra with a setpoint of $U_b = 1.5$ V, $I_T = 100$ pA. B) Tunneling spectra recorded at different tip-sample distances defined by the set-point current ($U_b = 1.5$ V). The color code is the same as in Figure 8. Inset: STM image of WDS-2 on Au(111) with the position of the tip marked in blue (50×50 nm²).

determined value $\Delta E_{\text{HOMO-LUMO}}$ of 1.94 eV, reflecting the band gap of the trimethylolethane-ligated $\{P_2V_3W_{15}O_{59}\}$ -type POM,^[47] compares well to $E_{G2}(\text{WDS-1}) = 1.83$ eV obtained experimentally for WDS-1 in the second layer on the Au(111) surface. This indicates that WDS-1 polyoxoanions with no direct contact with the metallic surface are fully oxidized.

These data indeed prompted us to revisit the XPS measurements performed for $(\text{TBA})_3\text{WDS-1}$ and $(\text{TBA})_3\text{WDS-2}$ in order to understand the relatively small band gaps of almost equal size, which were determined experimentally for the title polyoxoanions on Au(111). The V 2p core level spectra of WDS-1 and WDS-2 on gold clearly indicate the presence of V^{IV} , pointing to a spontaneous reduction of POM on this metallic surface. These data are in agreement with direct observation of a band gap decrease, when WDS-1 moves from the second layer into the first adsorption layer and gets into contact with Au(111) during the I - V measurements, like recorded several times in

STM/STS experiments (see above Figure 9C). During contact formation, the energy levels of WDS-1 align with the Fermi level of Au(111) ($E_F(\text{Au})$) and a redistribution of charges can be established. This charge transfer from Au(111) to the most electronegative transition-metal acceptor, that is, vanadium, implies that the LUMO, initially located mainly at V^V in the V_3 -cap region of electrically isolated WDS-1 in the second adsorption layer,^[48] falls below $E_F(\text{Au})$. As a result, the former LUMO becomes the HOMO, which is located at the now reduced V^{IV} of WDS-1 in contact with the metallic surface. The band gaps of WDS-1 and WDS-2 adsorbed directly on Au(111) are thus defined by the HOMO located at the vanadium atoms in the V_3 -cap region and the LUMO formed by the tungsten atoms in the belt region of the POMs.^[48] At the same time, this is the reason for the almost equal sized band gaps of both title POMs, as their ligands exert diminished influence on already reduced V^{IV} atoms, that is, the possibility of charge transfer is reduced. While fully-oxidized WDS-1 polyoxoanions located in the second adsorption layer exhibit an oxygen-to-transition metal band gap, those directly adsorbed on Au(111) are reduced and characterized by a band gap between two transition metals (V^{IV} in the cap region and W^{VI} in the belt region). Due to that, the STS characteristics changes upon adsorption and the band gap of the reduced WDS-1 gets smaller than that of the fully-oxidized polyoxoanions. These findings are in line with the reduction of Wells-Dawson-type POMs on Al and ITO substrates, as observed by Douvas et al.^[40]

Based on the STS measurements of the single WDS-1 and WDS-2 polyoxoanions (see Figure S10, Supporting Information) and given data from literature, we created schematic energy diagrams describing the electronic band structure of ligated and ligand-free $P_2V_3W_{15}$ -type POMs (Figure 11). In Figure 11A, the results of theoretical calculations on the ligand-free $[P_2V_3W_{15}O_{62}]^{9-}$ ^[48] and the related, ligated $[P_2V_3W_{15}O_{59}((\text{OCH}_2)_3\text{C-R})]^{6-}$ POMs with $R = \text{Me}$ and NH_2 ^[43] were aligned to the experimental results obtained for the ligand-free, fully-protonated $H_9[P_2V_3W_{15}O_{62}]$ ^[42] by leveling to a common oxo band. As can be seen from Figure 11A, the LUMO of ligated POMs, as reported in the literature for isolated POMs and realigned in the above-mentioned way, lies underneath $E_F(\text{Au})$. This indicates that a spontaneous reduction of WDS-1 and WDS-2 on the gold surface should be, in principle, energetically favorable.

Figure 11B schematizes the experimental STS data with respect to $E_F(\text{Au})$, obtained for WDS-1 and WDS-2. Here, the energy diagram shows that the size of the band gap determined for WDS-1 in the second adsorption layer is convincingly consistent with the calculated values for related, ligated POMs.^[47] However, the HOMO of both polyoxoanions, WDS-1 and WDS-2, directly adsorbed on Au(111) is located mainly on the reduced V_3 -cap and appears above the “oxo band”. As a consequence, the band gap is diminished and the “oxo band” corresponds to the HOMO-1 in the reduced POM.

Let us now consider the energy levels corresponding to the V_3 -cap and the oxo band of WDS-1 during reduction of V^V to V^{IV} (Figure 11B). The energy gap between the V_3 -cap (V^V) and the oxo band corresponding to 1.83 eV (HOMO-LUMO gap of WDS-1 in the second adsorption layer) and the gap between the V_3 -cap (V^{IV}) and the oxo band corresponding to 0.3 eV (HOMO-(HOMO-1)) gap of adsorbed WDS on Au(111)

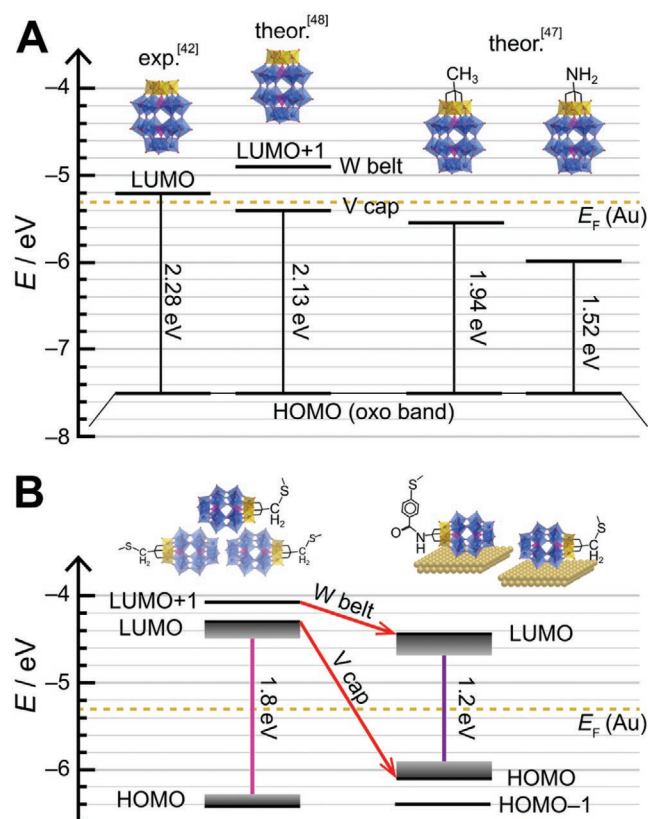


Figure 11. Schematic energy diagrams depicting the frontier molecular orbital regions for $P_2V_3W_{15}$ -type POMs. A) Comparison between the theoretical gap values of isolated POMs and an experimental gap value of $H_3[P_2V_3W_{15}O_{62}]$.^[42,47,48] B) Data derived from the STS measurements of WDS-1 and WDS-2 on Au(111). Left: WDS-1 from the second adsorption layer without direct contact with gold. Right: WDS-1 and WDS-2 in direct contact with gold. Gray bar represents the energy of the orbital peak onset to the peak maximum obtained from dI/dV curves. Golden dotted line emphasizes the Fermi level of Au(111).

can be related well to theoretically determined band gaps of simple vanadium oxides, that is, $E_G(V_2O_5) = 2.62$ eV and $E_G(VO_2) = 0.66$ eV, respectively.^[49] In both these cases a huge decrease of the energy gaps between the orbitals located at either V^V or V^{IV} atoms and the oxo band, amounting to ≈ 1.5 eV (POMs) and 2.0 eV (technical oxides), can be seen, an observation which greatly verifies our assumptions.

2.5. Switching Characteristics of WDS-1 and WDS-2 on Au(111)

The redox-dependent molecular electrical conductivity of WDS-1 and WDS-2 was investigated by cyclic I - V spectra and current-time (I - t) traces recorded with a fixed tip-sample distance defined by the set-point parameter. Switching phenomena were stochastically observed in I - V spectra, executed in the range +2.0 to -2.0 V, at negative sample bias voltages. **Figure 12A** shows a representative I - V spectrum of WDS-2 exhibiting a switching event at -1.7 eV with respect to $E_F(Au)$. The forward curve (black line) exhibits a sudden current increase of one order of magnitude (from 15 to 150 pA), which

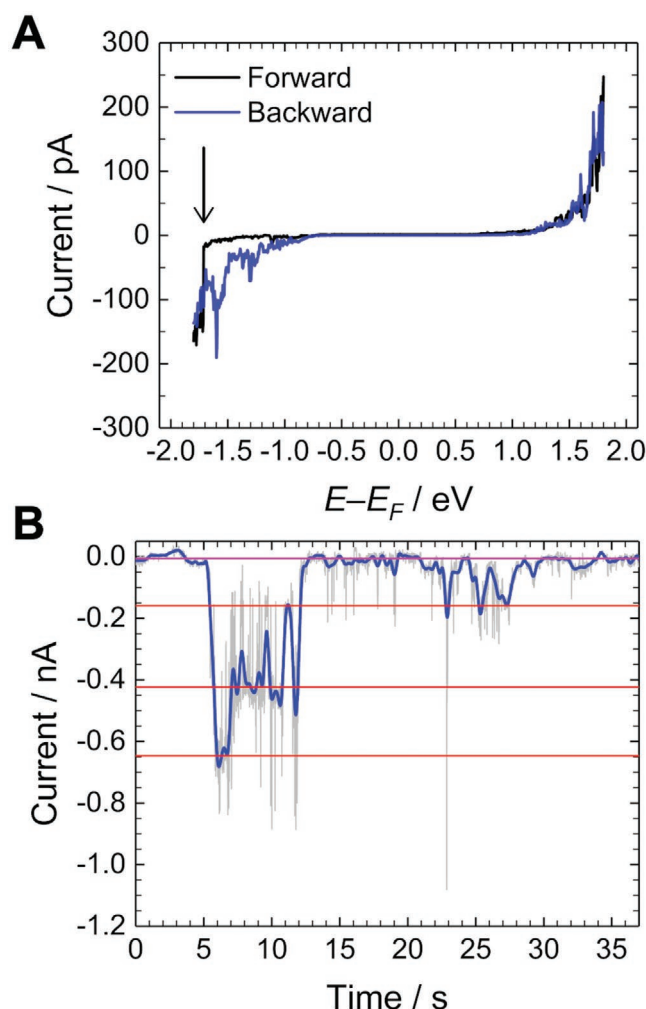


Figure 12. Switching events of WDS-2 on Au(111). A) Representative STS spectrum ($I_T = 200$ pA, $U_B = 1.8$ V). In the forward direction (black) the switching from a high-resistive state to a low-resistive state at -1.7 V is clearly discernible. B) Time-resolved resistive switching of WDS-2. A background subtracted I - t spectrum is shown. Three conductivity levels are emphasized by red lines ($I_T = 200$ pA, $U_B = -1.8$ V).

is characteristic of resistive switching. In the backward direction (blue line) the current decreases slowly to zero and follows at the positive sample voltage the forward direction. The comparison of our findings to literature data, for example, to vanadium oxide thin films with major V^{IV} valence contribution,^[50] reveals some analogies and size dependent differences. The WDS POMs as well as the thin films start in the high resistance state and need a voltage pulse to switch into the low resistance state. However, Rupp et al. find two kinds of volatile threshold switching and one type of non-volatile bipolar switching that can be addressed at voltages up to 1 V. This result is caused by the morphology of the thin films, which are amorphous or consist of amorphous and crystalline material and thus, enable different switching mechanisms. On the contrary, the WDS POMs possess a highly defined scaffold, so that changes of the cluster resistance should be caused by distinct variations of the charge state or the geometry of the constituting atoms.

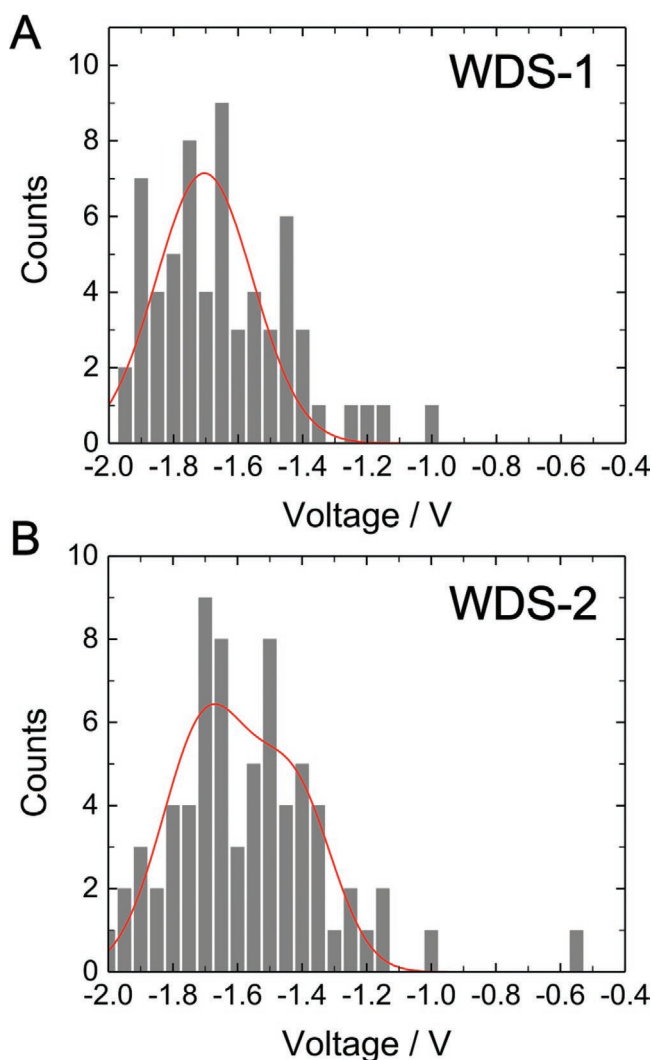


Figure 13. Statistics of the switching events for WDS-1 in (A) and for WDS-2 in (B). Red curve: Gaussian.

Besides in cyclic I - V spectra switching events are discovered likewise in time-resolved current measurements at fixed voltage values exhibiting sudden conductance changes in rather uniform steps. Figure 12B represents such a current-time trace depicting the switching between the initial state (magenta baseline) and three different conductance states (red lines) of WDS-2 on Au(111), thus indicating a multi-level switching.

A statistical evaluation of the switching characteristics based on 70 and 63 switching events of WDS-1 and WDS-2, respectively, is given in **Figure 13**. It provides for both POMs a maximum of the switching voltage roughly in the voltage range of -1.4 to -1.9 V. If the statistical data were examined separately for the large and the small tip-sample distances, two different switching voltages were obtained for the large tip-sample distances, that is, small tip-WDS-2 interactions. These two maxima at (-1.48 ± 0.08) V and (-1.67 ± 0.07) V (Figure S11, Supporting Information) point to two different switching events, which are observed rarely in one curve.

Since WDS-1 and WDS-2 assembled on the Au(111) surface exhibit an almost identical band gap ($E_{G1}(\text{WDS-1}) = 1.19\text{ eV}$ and $E_{G1}(\text{WDS-2}) = 1.17\text{ eV}$, see Figures 8B and 10) and a comparable switching behavior (between -1.4 and -1.9 V, see Figure 13) within our statistics, it can be concluded that the tris(alkoxo) ligands $(\text{OCH}_2)_3\text{C-R}$ ($\text{R}=\text{CH}_2\text{SMe}$ and $\text{NHCO}_6\text{H}_4\text{SMe}$, respectively) of these POMs play a minor role for the edge states determining the band gap and during the resistive switching events. However, to fully understand the resistive switching characteristics of WDS-1 and WDS-2 it is important to keep in mind that the three vanadium atoms in the V_3 -cap of the POMs are in the reduced state V^{IV} , if there is a direct contact of the POMs with the Au(111) surface. Addressing the HOMO involving these vanadium atoms at negative voltages in the STM configuration will lead in a first step to an oxidation process, that is, $\text{V}^{\text{IV}} \rightarrow \text{V}^{\text{V}} + \text{e}^-$, thus enabling hole conduction through this HOMO. Note that an increase in the absolute current in Figure 12B corresponds to a lower resistance, and a variation of the current in three steps points to three distinct processes, with each based on a one-electron transfer. Thus, the process depicted in Figure 12B after 5 s can be attributed to the cap of three V^{IV} centers that are oxidized in one step, resulting in a 0.6 nA higher current, and consecutively reduced again over time (≈ 6 s). The same is valid for the switching curve in Figure 12A. The oxidation occurs at -1.7 V in the forward curve and subsequently, while the voltage is raised again, a stepwise reduction takes place, that is, the switching between different reduction states in the backward curve appears as a “large” noise. The oxidized state V^{V} is only stable at voltages < -1.7 V. The on/off ratio deduced for WDS-1 and WDS-2 amounts to ≈ 40 .

3. Conclusion

We successfully synthesized and characterized two tris(alkoxo)-ligated WD-type polyoxoanions $[\text{HP}_2\text{V}_3\text{W}^{\text{VI}}_{15}\text{O}_{59}((\text{OCH}_2)_3\text{C-R})]^{5-}$ with $\text{R}=\text{CH}_2\text{SMe}$ (WDS-1) and $\text{NHCO}_6\text{H}_4\text{SMe}$ (WDS-2). The adsorption and the electronic properties of these hybrid POMs were investigated in detail on the Au(111) surface by real-space topographic, reciprocal space X-ray scattering, integral and local spectroscopic methods. We could show that the ligand functionality has a significant influence on the self-assembly of WDS-1 and WDS-2 on the metallic substrate. The WDS-2 polyoxoanion with a longer ligand chain and a higher degree of substitution affords larger assemblies of uniform height, due to the excellent ability to implement interactions via hydrogen bonds. By contrast, the WDS-1 polyoxoanion with a shorter ligand chain tends to form small islands on Au(111), which exhibit a considerable growth vertically. These findings open up new avenues to design and control the spatial distribution of WD-type polyoxoanions by fine-tuning of the POM-surface and POM-POM interplay through the ligand functionality.

Furthermore, we succeeded to establish experimentally the relationship between the electronic structure of the title POMs and their on-surface adsorption that determines the redox state of POM's vanadium centers. While WDS-1 in the second adsorption layer behaves as an isolated, fully-oxidized polyoxoanion exhibiting a band gap similar to the ones predicted theoretically for the related WD-type POMs, the situation

is completely different for the polyoxoanions being in direct contact with Au(111). In the first adsorption layer the vanadium centers of both WDS-1 and WDS-2 are reduced, and their band gap is considerably decreased. The re-oxidation of vanadium atoms in the V_3 -cap of these POMs at negative voltages in STM configuration results in a decrease of the resistivity and renders resistive switching of the WD-type POMs possible. As a result, we discovered a ligand-independent multi-electron switching orchestrated by the vanadium centers of WDS-1 and WDS-2, with an on/off ratio up to 40 and a hole conduction through the HOMO in the higher conductive state. This performance shows impressively the opportunities of POMs with V(3d) states as resistive switches. Further improvement of the stability of the switching process, like the adjustment of the substrate Fermi-level or the electron donating ability of the ligands, will be necessary to enable the integration of such POMs with practical electronic devices.

4. Experimental Section

Surface Sample Preparation: For XPS, XRR, and GISAXS measurements, template stripped gold chips from AMS Biotechnology (Europe) Ltd were used. After cleaving the $1 \times 1 \text{ cm}^2$ chip from the wafer, 20 μL of an 80 μM POM solution in acetonitrile was deposited on the surface and dried under acetonitrile saturated vapor. For AFM, STM, and STS measurements, crystalline Au(111) films (layer thickness of 200 nm) deposited on mica substrates in a two-step deposition process as described elsewhere^[51] were used. To create a comparable covering, relative to the XPS, XRR and GISAXS samples, the same amount of the 80 μM POM solution was used on the Au(111) surfaces according to the respective area of the substrates. For STM and STS investigations also samples with a 1:3 lower covering were employed. All solutions were freshly prepared using dry acetonitrile. In each case the solution was deposited on the gold surface, dried under acetonitrile saturated vapor, and subsequently the samples were transferred into ultra-high vacuum.

X-Ray Photoelectron Spectroscopy: XPS measurements were recorded on a PHI 5000 Versa Probe (Physical Electronics Inc., USA). The base pressure was 1×10^{-9} mbar. An Al $K\alpha$ source (1486.6 eV) with monochromator was used. A pass energy of 58.7 eV and an analyzer angle of 45° were chosen. An energy step size of 0.125 eV was used for the vanadium and oxygen region, and a step size of 0.25 eV for the other regions. All measurements were carried out without a neutralization mode. With CasaXPS the spectra were analyzed and fitted to a convolution of a Lorentz and a Gaussian profile after subtraction of a Shirley-type background. For the nitrogen region a linear background was used. The binding energies were controlled by the Au 4f peak at 83.95 eV. There was no need for energy shifting. To ensure that there was no charge-induced shifting over time, the Au 4f and the W 4f core level regions were recorded before and after the long measurement of the vanadium region.

Grazing-Incidence Small-Angle Scattering and X-Ray Reflectivity: The GISAXS and XRR measurements were performed with a GALAXI diffractometer^[52] (Jülich Centre for Neutron Science, Forschungszentrum Jülich). A METALJET X-ray source (0.13414 nm radiation wavelength) and a Pilatus 1M 2D position sensitive detector were used. The incoming beam with a collimation of 0.25 mrad in both directions perpendicular to its flight path has a size of $0.7 \times 0.7 \text{ mm}^2$ at sample position. The samples were prepared under ambient conditions and then placed in a vacuum sample chamber (base pressure $\approx 10^{-1}$ mbar) and measured at ambient temperature. The reflected and scattered intensities were recorded at a sample-to-detector distance of 0.83 m. For the XRR measurements, special care was taken to subtract the signal of off-specular scattering located at the same place as the specular reflection.

Scanning Probe Microscopy: For the AFM, STM, and STS measurements a commercial VT-SPM from Scienta Omicron was used. The scans were recorded at ambient temperature with a base pressure $< 1 \times 10^{-9}$ mbar. The non-contact AFM measurements were performed in the frequency modulation mode with a doped silicon cantilever (S.I.S Surface Imaging Systems, Germany) with a nominal tip radius $< 7 \text{ nm}$ and a resonance frequency of $f_R = 158 \text{ kHz}$. In this mode the cantilever is oscillating at a constant amplitude of $\approx 4 \text{ nm}$. For distance control the shift in the resonance frequency (Δf), induced by surface–tip interaction, was used. A bias voltage was supplied to minimize the electrostatic forces.^[53] The STM and STS experiments were performed with electrochemically etched tungsten tips. The tunneling current for the STM images described herein was 10 pA and the tip bias voltage was 1.5 V. For spectroscopy the tip was moved over the chosen measurement point, the tip–surface distance was adjusted via the set-point current and voltage, the feedback loop was turned off, and the I – V spectra were recorded. The obtained images were plane corrected and partially filtered with a gentle median filter using the SPIP 6.0.13 software from Image Metrology. The obtained I – V curves were evaluated with OriginPro 2017G.

Statistical Analysis: The data for the statistical analyses of the switching events were used without pre-processing. A standard deviation corresponding to one sigma is given where applicable in the text. The statistical analyses are based on data sets comprising more than 60 events, like given in the text. Multiple Gaussian fits were applied to the data sets and only for separations larger than two sigma separated peaks were accepted. The employed software was OriginPro 2017G.

Supporting Information

Supporting Information is available from the Wiley Online Library or from the author.

Acknowledgements

This work was supported by the Leibniz Association through the Leibniz Collaborative Excellence funding program (iMolKit). S.K. thanks the funding of Deutsche Forschungsgemeinschaft (DFG) through SFB 917 “Nanoswitches”.

Open access funding enabled and organized by Projekt DEAL.

Conflict of Interest

The authors declare no conflict of interest.

Data Availability Statement

Research data are not shared.

Keywords

electronic band gaps, polyoxometalates, scanning probe techniques, surface engineering, vanadium

Received: March 1, 2022

Revised: May 19, 2022

Published online: June 27, 2022

[1] G. E. Moore, *IEEE Solid-State Circuits Soc. Newslett.* **2006**, 11, 33.

[2] A. Sebastian, M. Le Gallo, R. Khaddam-Aljameh, E. Eleftheriou, *Nat. Nanotechnol.* **2020**, 15, 529.

- [3] IEEE, International Roadmap for Devices and Systems: 2021, <https://irds.ieee.org/editions/2021> (accessed: February 2021)
- [4] H. Chen, J. Fraser Stoddart, *Nat. Rev. Mater.* **2021**, 6, 804.
- [5] P. T. Mathew, F. Fang, *Engineering* **2018**, 4, 760.
- [6] T. Hasegawa, K. Terabe, T. Tsuruoka, M. Aono, *Adv. Mater.* **2012**, 24, 252.
- [7] S. Gao, X. Yi, J. Shang, G. Liu, R. W. Li, *Chem. Soc. Rev.* **2019**, 48, 1531.
- [8] R. Waser, M. Aono, *Nat. Mater.* **2007**, 6, 833.
- [9] B. Hu, C. Wang, J. Wang, J. Gao, K. Wang, J. Wu, G. Zhang, W. Cheng, B. Venkateswarlu, M. Wang, P. S. Lee, Q. Zhang, *Chem. Sci.* **2014**, 5, 3404.
- [10] R. Waser, R. Dittmann, G. Staikov, K. Szot, *Adv. Mater.* **2009**, 21, 2632.
- [11] I. Valov, *ChemElectroChem* **2014**, 1, 26.
- [12] S. H. Jo, T. Chang, I. Ebong, B. B. Bhadviya, P. Mazumder, W. Lu, *Nano Lett.* **2010**, 10, 1297.
- [13] T. Ohno, T. Hasegawa, T. Tsuruoka, K. Terabe, J. K. Gimzewski, M. Aono, *Nat. Mater.* **2011**, 10, 591.
- [14] M. Moors, K. K. Adepalli, Q. Lu, A. Wedig, C. Bäumer, K. Skaja, B. Arndt, H. L. Tuller, R. Dittmann, R. Waser, B. Yildiz, I. Valov, *ACS Nano* **2016**, 10, 1481.
- [15] A. Wedig, M. Luebben, D.-Y. Cho, M. Moors, K. Skaja, V. Rana, T. Hasegawa, K. K. Adepalli, B. Yildiz, R. Waser, I. Valov, *Nat. Nanotechnol.* **2016**, 11, 67.
- [16] A. Sawa, *Mater. Today* **2008**, 11, 28.
- [17] X. Chen, Y. Zhou, V. A. L. Roy, S. Han, *Adv. Mater.* **2018**, 30, 1703950.
- [18] M. Moors, J. Warneke, X. López, C. De Graaf, B. Abel, K. Y. Monakhov, *Acc. Chem. Res.* **2021**, 54, 3377.
- [19] D.-L. Long, R. Tsunashima, L. Cronin, *Angew. Chem., Int. Ed.* **2010**, 49, 1736.
- [20] A. V. Anyushin, A. Kondinski, T. N. Parac-Vogt, *Chem. Soc. Rev.* **2020**, 49, 382.
- [21] G. Izzet, F. Volatron, A. Proust, *Chem. Rec.* **2017**, 17, 250.
- [22] L. Vilà-Nadal, S. G. Mitchell, S. Markov, C. Busche, V. Georgiev, A. Asenov, L. Cronin, *Chem. – A Eur. J.* **2013**, 19, 16502.
- [23] C. Busche, L. Vilà-Nadal, J. Yan, H. N. Miras, D.-L. L. Long, V. P. Georgiev, A. Asenov, R. H. Pedersen, N. Gadegaard, M. M. Mirza, D. J. Paul, J. M. Poblet, L. Cronin, *Nature* **2014**, 515, 545.
- [24] K. Y. Monakhov, M. Moors, P. Kögerler, *Polyoxometalate Chemistry* (Eds.: R. vanEldik, L. Cronin), vol. 69, Academic Press, Amsterdam **2017**, pp. 251.
- [25] M. Laurans, K. Dalla Francesca, F. Volatron, G. Izzet, D. Guerin, D. Vuillaume, S. Lenfant, A. Proust, *Nanoscale* **2018**, 10, 17156.
- [26] Q. Zhu, B. Paci, A. Generosi, S. Renaudineau, P. Gouzerh, X. Liang, C. Mathieu, C. Rountree, G. Izzet, A. Proust, N. Barrett, L. Torte, *J. Phys. Chem. C* **2019**, 123, 1922.
- [27] X. Chen, P. Huang, X. Zhu, S. Zhuang, H. Zhu, J. Fu, A. S. Nissimagoudar, W. Li, X. Zhang, L. Zhou, Y. Wang, Z. Lv, Y. Zhou, S.-T. Han, *Nanoscale Horiz.* **2019**, 4, 697.
- [28] N. S. Sterin, N. Basu, M. Cahay, M. N. Satyanarayan, S. S. Mal, P. P. Das, *Phys. Status Solidi A* **2020**, 217, 2000306.
- [29] O. Linnenberg, M. Moors, A. Notario-Estévez, X. López, C. de Graaf, S. Peter, C. Baeumer, R. Waser, K. Y. Monakhov, *J. Am. Chem. Soc.* **2018**, 140, 16635.
- [30] O. Linnenberg, M. Moors, A. Solé-Daura, X. López, C. Bäumer, E. Kentzinger, W. Pyckhout-Hintzen, K. Y. Monakhov, *J. Phys. Chem. C* **2017**, 121, 10419.
- [31] M. Glöß, R. Pütt, M. Moors, E. Kentzinger, W. Pyckhout-Hintzen, K. Y. Monakhov, *Nanoscale* **2019**, 11, 4267.
- [32] R. G. Finke, B. Rapko, R. J. Saxton, P. J. Domaille, *J. Am. Chem. Soc.* **1986**, 108, 2947.
- [33] T. H. Fleisch, G. J. Mains, *J. Chem. Phys.* **1982**, 76, 780.
- [34] J. Gong, R. N. Hua, Z. W. Xie, S. G. Wang, L. Y. Qu, *Polym. J.* **2001**, 33, 377.
- [35] C. Chen, G. Chen, H. Yang, G. Zhang, D. Hu, H. Chen, T. Guo, *J. Mater. Chem. C* **2017**, 5, 9273.
- [36] J. Mendialdua, R. Casanova, Y. Barbaux, *J. Electron Spectrosc. Relat. Phenom.* **1995**, 71, 249.
- [37] S. Frey, A. Shaporenko, M. Zharnikov, P. Harder, D. L. Allara, *J. Phys. Chem. B* **2003**, 107, 7716.
- [38] X. Li, T. Zheng, X. Liu, Z. Du, X. Xie, B. Li, L. Wu, W. Li, *Langmuir* **2019**, 35, 4995.
- [39] M. Stuckart, K. Y. Monakhov, *Encyclopedia of Inorganic and Bioinorganic Chemistry*, (Ed.: R. A. Scott), John Wiley & Sons, Ltd, Chichester, UK **2018**, pp. 1.
- [40] A. M. Douvas, D. Tsikritzis, C. Tselios, A. Haider, A. S. Mougharbel, U. Kortz, A. Hiskia, A. G. Coutsolelos, L. C. Palilis, M. Vasilopoulou, S. Kennou, P. Argitis, *Phys. Chem. Chem. Phys.* **2019**, 21, 427.
- [41] H. B. Michaelson, *J. Appl. Phys.* **1977**, 48, 4729.
- [42] J.-S. Li, X.-J. Sang, W.-L. Chen, L.-C. Zhang, Z.-M. Zhu, T.-Y. Ma, Z.-M. Su, E.-B. Wang, *ACS Appl. Mater. Interfaces* **2015**, 7, 13714.
- [43] C. P. Pradeep, D.-L. Long, G. N. Newton, Y.-F. Song, L. Cronin, *Angew. Chem., Int. Ed.* **2008**, 47, 4388.
- [44] L. G. Parratt, *Phys. Rev.* **1954**, 95, 359.
- [45] S. Disch, E. Wetterskog, R. P. Hermann, G. Salazar-Alvarez, P. Busch, T. Brückel, L. Bergström, S. Kamali, *Nano Lett.* **2011**, 11, 1651.
- [46] R. M. Feenstra, *J. Vac. Sci. Technol. B: Microelectron. Process. Phenom.* **1987**, 5, 923.
- [47] T. Zhang, L.-K. Yan, S. Cong, W. Guan, Z.-M. Su, *Inorg. Chem. Front.* **2014**, 1, 65.
- [48] X. López, C. Bo, J. M. Poblet, *J. Am. Chem. Soc.* **2002**, 124, 12574.
- [49] N. Szymanski, Z. Liu, T. Alderson, N. Podraza, P. Sarin, S. Khare, *Comput. Mater. Sci.* **2018**, 146, 310.
- [50] J. A. J. Rupp, M. Querré, A. Kindsmüller, M.-P. Besland, E. Janod, R. Dittmann, R. Waser, D. J. Wouters, *J. Appl. Phys.* **2018**, 123, 044502.
- [51] B. Lüssem, S. Karthäuser, H. Haselier, R. Waser, *Appl. Surf. Sci.* **2005**, 249, 197.
- [52] E. Kentzinger, M. Krutyeva, U. Rücker, *J. Large-Scale Res. Facil. JLSRF* **2016**, 2, A61.
- [53] F. J. Giessibl, *J. Appl. Phys.* **1994**, 33, 3726.